Pergamon

PII: S0968-4328(97)00033-4

Micron Vol. 28, No. 5, pp. 333–348, 1997
Published by Elsevier Science Ltd. Printed in Great Britain
0968-4328/97 $17.00+0.00

EELS in the STEM: Determination of Materials Properties on the Atomic Scale

N. D. BROWNING,* D. J. WALLIS,*‡ P. D. NELLIST†§ and S. J. PENNYCOOK†

**Department of Physics (M/C 273), University of Illinois at Chicago, 845 West Taylor Street, Chicago, IL, 60607-7059, U.S.A.*
†Solid State Division, Oak Ridge National Laboratory, Bethel Valley Road, Oak Ridge, TN, 37831-6030, U.S.A.

(*Received* 1 *April* 1997; *accepted* 2 *June* 1997)

Abstract—By performing EELS in conjunction with the Z-contrast imaging technique in the scanning transmission electron microscope (STEM), detailed information on the composition, chemistry and structure of materials can be obtained with atomic resolution and sensitivity. This unprecedented resolution can be achieved by using an atomic resolution Z-contrast image to first identify structural features of interest and then to position the electron probe over the feature for spectral acquisition. This method greatly limits the number of spectra that need to be acquired from a given specimen, thus reducing total acquisition time and specimen stability problems. In addition, a key advantage of this methodology is that the collection conditions for the spectrum can be tailored to produce an incoherent, atomic resolution spectrum that can be correlated directly with the image. This means the image can be used as a reference atomic structure for theoretical modeling of the spectral fine-structure. Using multiple scattering analysis, the reference structure can be modified to reproduce the experimental spectrum, thus giving a 3-dimensional structural determination that is sensitive to single atom vacancies and impurities. In this paper, the application of this combined EELS and Z-contrast technique to various materials problems is described. In the case of the MBE growth of CdTe on Si, the combined atomic resolution techniques allow the diffusion of Te into the silicon substrate to be identified and a novel graphoepitaxial growth mechanism to be identified. For nanoscale iron particles used as a fuel additive to reduce/enhance soot formation during combustion, measurement of the distribution of iron oxidation states within the particles permits a mechanism for soot formation to be proposed. The application of the multiple scattering analysis techniques to the study of grain boundaries is described for tilt boundaries in TiO_2 and $SrTiO_3$. In both cases, the multiple scattering analysis gives information not present in the image and allows the 3-dimensional structure of each boundary to be determined.

Key words: STEM, EELS, Z-contrast imaging, interfaces, defects, nanoscale particles.

INTRODUCTION

Electron energy loss spectroscopy (EELS) has been demonstrated to have a wide variety of analytical applications, such as the determination of the dielectric constant, composition, band structure and chemistry (Egerton, 1986; Disko *et al.*, 1992). However, for many modern materials, the fluctuations in the composition, structure and chemistry that can limit the bulk properties occur on the atomic scale. To understand fully the properties of these materials and the performance of subsequent device applications, it is therefore essential to be able to perform spectroscopy with both atomic spatial resolution and single atom compositional sensitivity. One means of obtaining this unprecedented resolution and sensitivity is through the use of a scanning transmission electron microscope (STEM).

In the dedicated STEM, the electron optics are designed to form a small electron probe on the surface of the specimen (Fig. 1). As the probe is scanned over the surface of the specimen, the scattered electrons are collected in multiple imaging and analytical detectors (Fig. 1). For imaging, the integrated output from either of the detectors is displayed on a TV screen scanning synchronously with the probe as it is moved over the surface of the specimen. As can be seen from Fig. 1, images can be acquired simultaneously with microanalysis, thereby allowing them to be used to position the probe accurately for spectroscopy. This ability of the STEM to provide a reference image, makes it a very powerful instrument for microanalysis at high-spatial resolution.

The use of a dedicated STEM to obtain high spatial resolution EELS from materials is not new (Brown, 1981; Colliex and Mory, 1984). However, a major breakthrough leading to the eventual attainment of atomic resolution spectra, was the development of the Z-contrast imaging technique for crystalline materials (Pennycook and Boatner, 1988). For crystalline materials in zone axis orientations, when the probe size is smaller than the atomic spacing, the Z-contrast image forms a directly interpretable image of the atomic structure in which the contrast is proportional to the atomic number of the elements under the electron beam. This means that atomic columns in the image can be identified in real time and used as a map to position the electron probe for spectroscopy. In addition to positioning the probe with atomic accuracy, the local atomic structure around the probe is now known, at least in projection, thus greatly reducing the difficulties associated with spectral interpretation.

‡D. J. Wallis, Present address: DERA Malvern, Malvern, Worcs, U.K.
§P. D. Nellist, Present address: Cavendish Laboratory, U. Cambridge, Cambridge, UK

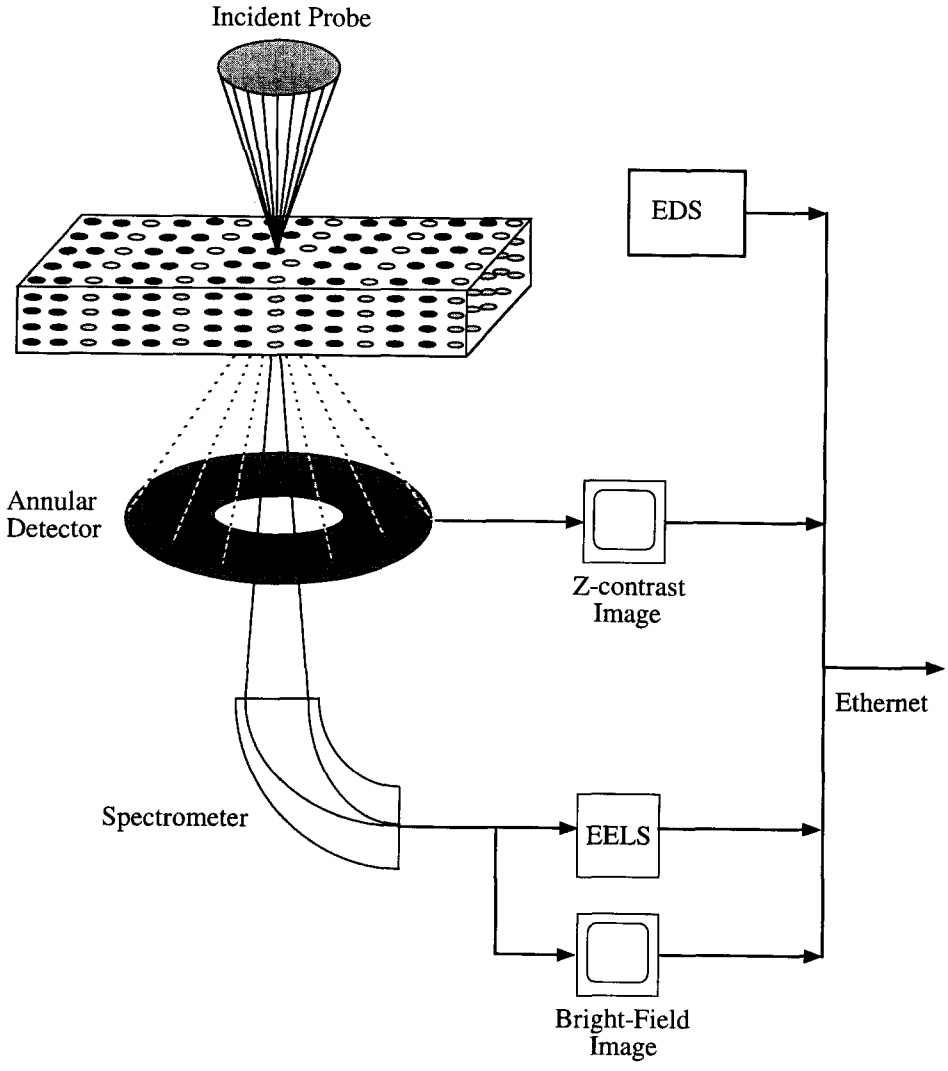

Fig. 1. Schematic of the STEM.

For complete correlation with the Z-contrast image it is necessary that the spectra have the same atomic resolution. As can be seen from Fig. 1, provided there is no probe broadening, the resolution of both the spectrum and image in the STEM is primarily governed by the probe size. Therefore, if an atomic resolution Z-contrast image is obtained and the inelastic interaction is sufficiently localized at the atomic cores, i.e. less than the atomic spacing, atomic resolution spectroscopy is possible. In practice this is achieved by limiting the region of the spectrum being investigated to the core-loss regime (>100 eV) (Browning and Pennycook, 1993). Obviously, if only core-losses are being investigated the signal levels are extremely low and an efficient CCD based detection system must be employed (McMullan *et al.*, 1990). However, it must be remembered that the Z-contrast image is obtained scanning close to normal TV rates and this image of the atomic structure is what is used to determine the positions from which spectra are obtained. Thus, as no attempt is being made to generate an EELS image, the number of spectra being acquired is very small and the time to acquire them limited to only a few seconds. This greatly reduces the problems of specimen drift and beam damage that are normally associated with detecting small signal levels. Another advantage of this methodology, again as no attempt is being made to form an image, is that a large collection angle can be used. As in the case of the Z-contrast image, a large collection angle averages any coherency that may exist in the energy loss signal leading to a simple quantitative interpretation of the energy-loss spectrum. In addition, this average over a large collection angle effectively removes the orientation or channeling effects from the spectrum that have been observed in previous TEM studies (Taftø and Krivanek, 1982).

In this paper, the methodology behind the use of Z-contrast imaging and EELS in combination is described in detail and several applications for materials science are discussed. The three applications represent examples of these techniques being used to determine composition, chemistry and structure fluctuations with atomic resolution and sensitivity. A major advantage of these correlated techniques in providing sufficient information to propose mechanisms leading to the observed structure-properly relationships is highlighted by these applications.

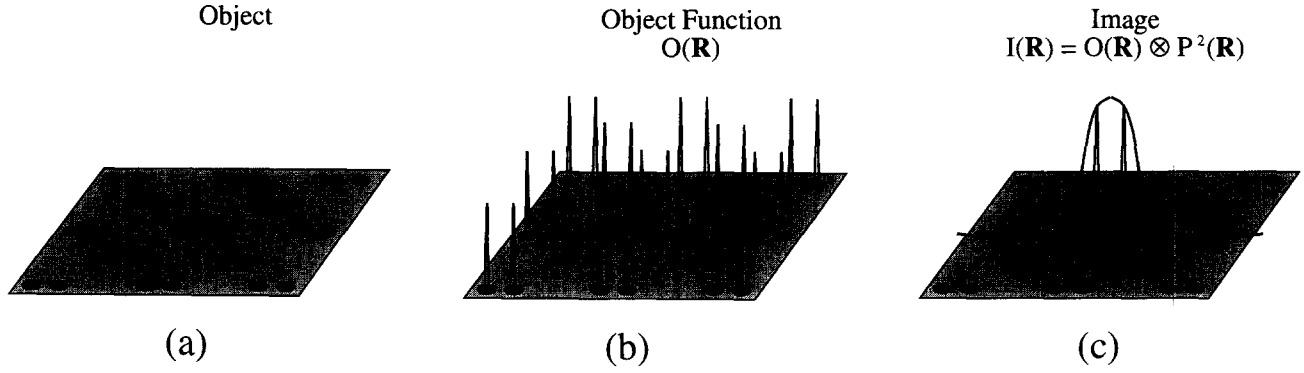

Fig. 2. The specimen consists of an array of atomic columns (a) for which the potential for high-angle scattering can be represented by an object function (b). The experimental image can be interpreted as a simple convolution of the experimental probe and the object function (c).

EXPERIMENTAL TECHNIQUES

Z-contrast imaging

Z-contrast images (Pennycook and Boatner, 1988; Pennycook and Jesson, 1990; Loane *et al.*, 1992) are formed by collecting the high-angle scattering (75–150 mrad at 100 kV) on an annular detector (Fig. 1). Detecting the scattered intensity at these high-angles and integrating over a large angular range effectively averages coherence effects between neighboring atomic columns in the specimen. Thermal vibrations reduce the coherence between atoms in the same column to residual correlations between near neighbors (Jesson and Pennycook, 1993), a second order effect. This allows each atom to be considered as an independent scatterer. Scattering factors may be replaced by cross sections, and these approach a Z^2 dependence on atomic number. This cross-section effectively forms an object function that is strongly peaked at the atom sites, so for very thin specimens where there is no dynamical diffraction, the detected intensity consists of a convolution of this object function with the probe *intensity* profile (Fig. 2). The small width of the object function ($\sim$0.02 nm) means that the spatial resolution is limited only by the probe size of the microscope. For a crystalline material in a zone-axis orientation, where the atomic spacing is greater than the probe size, the atomic columns are illuminated sequentially as the probe is scanned over the specimen. An atomic resolution compositional map is thus generated, in which the intensity depends on the average atomic number of the atoms in the columns.

This result also holds true for thicker specimens. It has previously been noted that for specimens in zone-axis orientations, the STEM probe forms narrow spikes around the atomic columns as it propagates (Fertig and Rose, 1981; Loane *et al.*, 1988). This effect is caused by the coherent nature and large angular spread of the STEM probe, which leads to the tightly bound s-type Bloch states adding constructively and the less localized states interfering destructively (Pennycook and Jesson, 1991). This effect is enhanced for scattering processes such as high-angle thermal diffuse scattering that are localized at the atomic cores, causing a great reduction in beam broadening. With only one dominant Bloch state, dynamical diffraction effects are largely removed and manifest only as a columnar channeling effect, thus maintaining the thin specimen description of the image as a simple convolution of the probe intensity profile and an object function, strongly peaked at the atom sites (Fig. 2).

The phase problem associated with the interpretation of conventional high-resolution TEM images is therefore eliminated. In thin specimens, the dominant contribution to the intensity of a column is always its composition, although due to the higher absorption of the heavy strings the contrast does decrease with increasing specimen thickness and in very thick crystals there is no longer a high resolution image. The effect of changing focus is also intuitively understandable as the focus control alters the probe intensity profile on the surface of the specimen. For defocus less than the optimum Scherzer condition, the probe broadens causing the individual columns not to be resolved. For higher defocus values the probe narrows with the formation of more intense tails, causing sharper image features but compositional averaging over several columns. The optimum focus condition therefore represents a compromise between high resolution (narrow probe profile) and the desire for a highly local image (no significant tails to the probe). This also corresponds to the optimum probe for microanalysis.

At defects and interfaces, structures can become extremely complicated causing difficulties in determining the precise 3-dimensional composition. However, provided an atomic column is continuous through the crystal, reconstructions will only result in a change in column intensity and not a contrast reversal. The atomic structure in the region of defects and interfaces can therefore still be determined largely from the image, and used as a map to position the electron probe for EELS (Browning *et al.*, 1993; Batson, 1993). Using the energy loss spectrum, the full 3-dimensional determination can be achieved (see later).

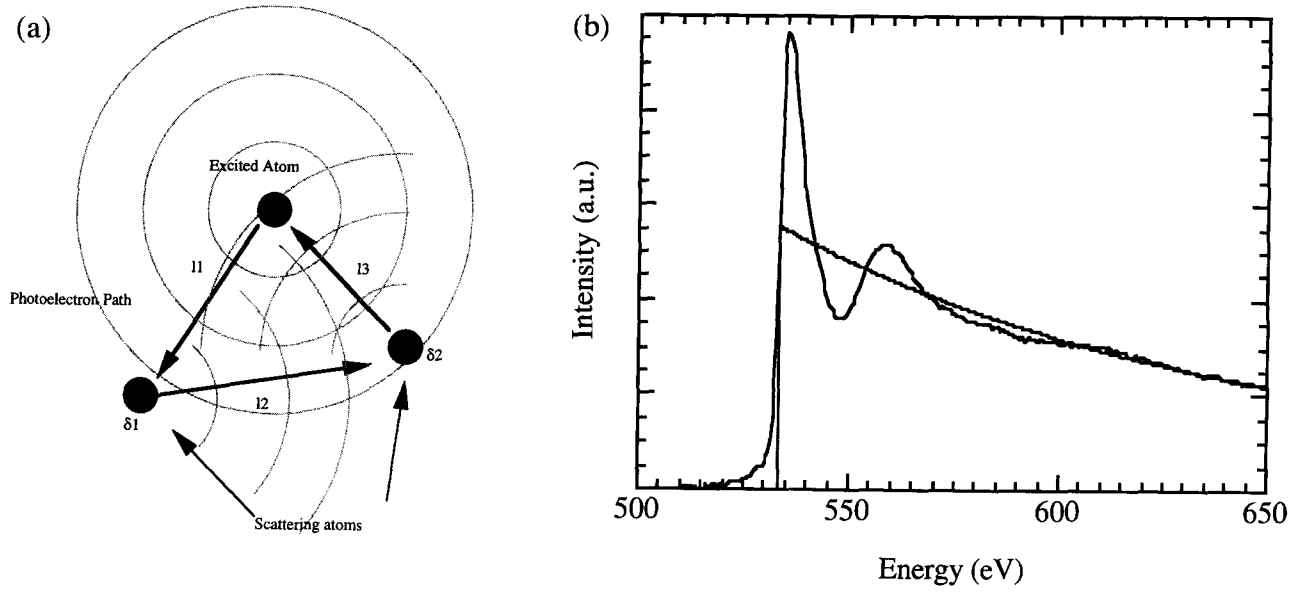

Fig. 3. (a) Schematic of the scattering of the photoelectron wave from surrounding atoms. (b) the interference effects lead to a modulation of the K-edge intensity.

Electron energy loss spectroscopy

As can be seen from Fig. 1, the annular detector used for Z-contrast imaging does not interfere with the low-angle scattering used for electron energy loss spectroscopy. This means that the Z-contrast image can be used to position the electron probe over a particular structural feature for acquisition of a spectrum. To be able to correlate the spectrum precisely with the structural feature, it is essential that the spectrum have the same atomic resolution as the Z-contrast image. In order to achieve this atomic resolution, the range over which a fast electron can cause an excitation event must be less than the interatomic spacing. Hydrogenic models (Ritchie and Howie, 1988; Allen and Rossouw, 1990) show that for the majority of edges accessible by conventional energy-loss spectrometers (ΔE <2 keV) the object functions are localized within 0.1 nm of the atom cores (Pennycook *et al.*, 1995; Browning and Pennycook, 1996; Holbrook and Bird, 1995). Hence, like the Z-contrast image, we have an object function localized at the atom cores and an experimental probe of atomic dimensions. For crystalline materials in zone-axis orientations, providing we maintain a large collection angle (15–30 mrad), coherent effects will be averaged and the description of the spectrum in terms of a convolution of the probe with an object function is valid (Fig. 2). An important aspect of this experimental approach is that the probe channeling discussed for Z-contrast imaging will also preserve the spatial resolution of the energy loss spectrum, thereby allowing atomic resolution analysis to be achieved even with these large collection apertures.

This correlation of the image and the spectrum allows the image to be used as a structural model to interpret the fine-structure of the energy loss spectrum. There are several methods which may be employed to do this. The simplest approach is to assign the various features to molecular orbitals formed by the interaction of an atom with its nearest neighbors (Tossell, 1973). Molecular-orbital theory uses group theory to produce molecular orbitals from a linear combination of atomic orbitals. However, group theory relies heavily on the symmetry of a molecule and therefore does not cope well with low symmetry structures such as those found at grain boundaries. This approach also becomes very clumsy to apply to anything but the smallest cluster of atoms and so potentially significant contributions to the electronic structure from second and third neighbor atoms are difficult to include. The use of the symmetry-projected density of states as derived from band structure calculations (Rez, 1992) is at the other end of the analysis scale. Although such calculations potentially provide the most accurate representation of the band-structure, they also rely heavily on the symmetry of a system. While techniques which allow band structure calculations to be applied to disordered structures have been developed, they require the use of very large unit cells containing many atoms with periodic boundary conditions. As a result of these considerations the computation time for such calculations is prohibitive.

An alternative method of spectrum interpretation is through multiple scattering calculations. This methodology was originally developed for near-edge structure interpretation in X-ray absorption spectroscopy (XANES) (Koningsberger, 1987). Application to electron microscopy is possible since the theory of ELNES and XANES are exactly analogous; the absorption processes are identical—only the radiation used to excite the atoms is different. Multiple scattering calculations model the density of states by considering the scattering of the excited photoelectron from neighboring atoms. The different paths which may be taken by a photoelectron alter the matrix elements for a particular transition due to the constructive or destructive interference which occurs between the outgoing and returning photoelectron wave (Fig. 3). In effect, the resultant spectrum

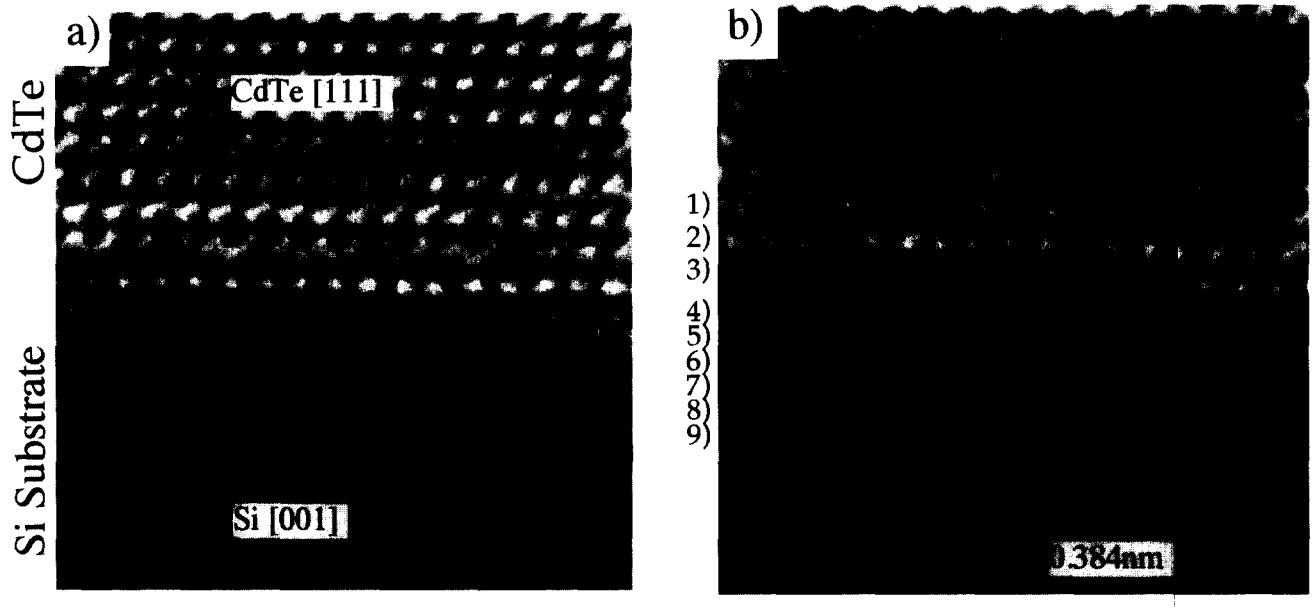

Fig. 4. (a) and (b): Z-contrast images of two regions along the same CdTe/Si interface.

may be described as a simple absorption edge of hydrogenic form, due to an isolated atom, with intensity modulations due to the structure of the solid (Fig. 3). i.e. the absorption $\alpha(E)$ is given by

$$\alpha(E)=\alpha_0(E)[1+\sum_{n=2} X_n(E)] \quad (1)$$

where $\alpha_0(E)$ is the atomic absorption and $X_n(E)$ is the multiple scattering signal of order n ($n>1$) which contains all the structural information (Benfatto *et al.*, 1986). Since this description of the density of states is based on a real space cluster of atoms, several unique opportunities are presented. The lack of symmetry no longer seriously affects the calculation and the effects of dopant atoms on ELNES may be simply investigated by substituting atom types within the cluster and recalculating the scattering. Additionally, by limiting the order of the terms included in the summation and the allowed scattering paths, the structural origins of particular features in the spectrum may be determined. Multiple scattering therefore allows spectral changes to be directly interpreted in terms of structural changes, and is ideal for the study of interfaces.

The multiple scattering calculations shown here were performed using commercial FEFF6 codes (Rehr *et al.*, 1992). These codes use the overlapping-atom prescription of Mattheiss (1964) to model the atomic potential within the muffin tin approximation. From the resulting potential, scattering phase shifts and matrix elements are calculated. Core-hole effects are included using the (Z+1)* approximation (Brydson *et al.*, 1992) where * denotes the excited atom. The curves shown are calibrated by alignment of the first spectral feature with experiment and broadening of 1 eV is added to allow direct comparison with experimental spectra. For the purposes of the calculation, the atomic clusters are divided into shells of atoms where a single shell is composed of atoms which lie between two radii about the excited site. The order of scattering is controlled simply by placing an upper limit on the number of scattering events which are allowed.

APPLICATIONS

All of the experimental energy loss spectra presented in this paper were obtained using a 100 kV VG HB501UX dedicated STEM. This microscope is fitted with a CCD based EELS detection system based on the design of McMullan *et al.* (1990). The optimum probe size for this microscope is 0.22 nm. Some of the Z-contrast images presented were obtained from a VG HB603U dedicated STEM, with a 0.126 nm optimum probe size.

Atomic resolution compositional profiles

The most straightforward application of the EELS and Z-contrast techniques is in determining composition profiles at heterophase interfaces. Heterophase interfaces are of particular importance in the MBE growth of advanced optoelectronic devices, where the nucleation of dislocations at the film-substrate interface can significantly limit device performance. One optoelectronic material of current interest is HgCdTe. In this material, the band gap can be tailored by the concentration of Hg, giving it applications as X-ray and γ-ray detectors and also in solar cell technology. An intriguing feature of this material is that it can be grown by MBE on Si substrates with a film quality comparable to bulk crystals, despite a 19.3% lattice mismatch (Chen *et al.*, 1995). This result is contrary to conventional ideas of heteroepitaxy, which suggest that such a large mismatch must inevitably lead to the nucleation of dislocations.

To investigate the mechanism which allows this single crystal growth, the film-substrate interface in the CdTe/Si system has been examined using Z-contrast imaging in a VG HB603U STEM and EELS in the VG HB501UX STEM. Fig. 4 shows Z-contrast images taken at different points along the same film/substrate interface. The CdTe film is easily identified since its atomic number is much higher than the Si substrate, giving it greater image intensity. The 0.126 nm spot size available in the HB603 STEM allows the atomic features in the [110] projection known as 'dumbbells' to be resolved in both silicon and CdTe. On careful inspection, the polarity of the CdTe dumbbell may be discerned in the bulk of the film. This polarity is constant right up to the CdTe/Si interface, showing that the film is Te initiated at the substrate. Comparing these images, two important features of the CdTe/Si interface become clear. Firstly, the Si termination differs by one monolayer but the orientation of the CdTe film remains the same. This demonstrates that the atomic structure of the Si surface is not controlling the epitaxial orientation; otherwise, the 90° rotation in symmetry of the substrate surface as it crosses a single height step would result in multi-domain growth. Secondly, it is clear that both interfaces are perfectly incommensurate, with no sign of localized dislocation cores. This is indicative of weak film/substrate bonding, and consistent with the large ($\sim$0.32 nm) spacing between the last Te plane in the film and the first plane of the substrate.

In the experimental Z-contrast images, atomic columns immediately below the film are seen to be bright, suggesting a significant concentration of a heavy element has substituted on to Si lattice sites. This element is confirmed to be tellurium by EELS spectra collected from the individual planes labeled in Fig. 4. The characteristic Te M45 core loss edge at 572 eV is detected approximately 4 planes into the Si surface, whereas the Cd core edge at 404 eV is only seen in the film (Fig. 5). This demonstrates that diffusion of Cd is extremely limited and also that the spatially extended Te signal does not occur due to instrumental or delocalization effects (Pennycook *et al.*, 1995). Additionally, Te is seen to be substitutional in both of the projections (Fig. 4), and due to its large size is presumably the origin of the extended dumbbell terminating the substrate with an interatomic spacing of 0.18 nm, larger than the 0.136 nm for bulk Si below. Some distortion of these lattice sites parallel to the interface is also seen in Fig. 4. This structure is in excellent agreement with STM studies of monolayer coverages of Te on Si(001) surfaces (Yoshikawa *et al.*, 1994).

An indication of the nature of the bonding between Si - Te and Te - Te at this interface is provided by *ab initio* charge density calculations for the compound $SiTe_2$, performed using the Cerius[2] code by Molecular Simulations Inc (Fig. 6). The bonding between Si and Te atoms is strongly directional, whereas the charge density between sheets of Te atoms is very low, indicating a non-directional Van der Waals interaction. Since the interplanar spacing of neighboring Te layers (0.315 nm) is similar to the distance between the Te terminated substrate surface and the first Te layer in the film, it would appear that during the MBE growth, the Te layer at the Si surface removes the strong directional bonding of the substrate allowing a free alignment of the CdTe layer immediately above it. This growth mechanism is known as graphoepitaxy or Van der Waals epitaxy, and results in the film having dislocation concentrations comparable to bulk crystals of CdTe (Wallis *et al.*, 1997a). Based on these results, it appears likely that the growth of other high quality single crystal films could be achieved through this mechanism. In particular, other group VI elements may also be effective in capping the substrate surface, allowing a range of II-VI compounds to be grown. It is also possible that such compounds may be used as buffer layers for the epitaxial growth of other materials, such as GaN, on dissimilar substrates.

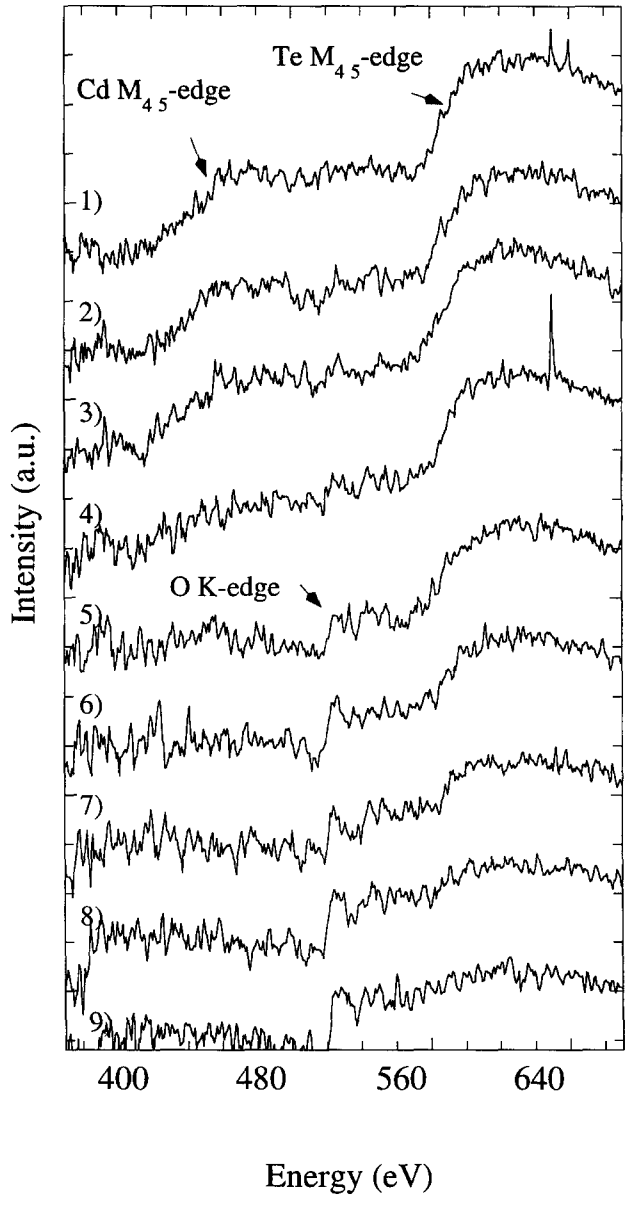

Fig. 5. Electron energy loss spectra collected from individual planes parallel to the CdTe interface. The numbered spectra correspond to the planes labeled in Fig. 4.

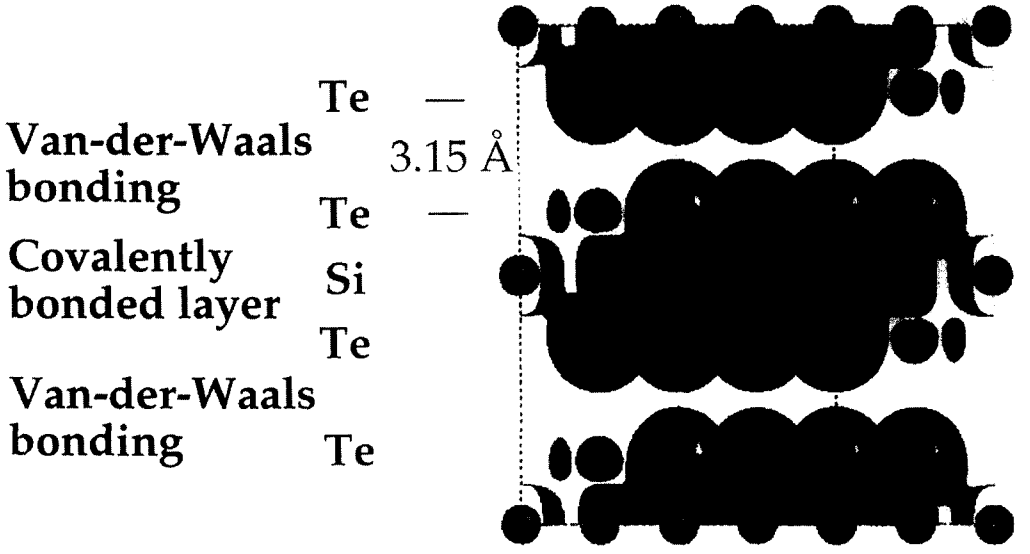

Fig. 6. Charge density plot for the layered $SiTe_2$ structure. Strong directional bonding is seen between Si and Te. The charge density between neighboring Te planes is very low indicative of Van der Waals type bonding.

Local chemistry fluctuations

Iron organometalic compounds have been shown to suppress carbonaceous soot emissions under certain conditions and are used as additives in combustion applications to control the production of combustion generated particulates. Practical applications of this technology include the production of carbon black, the base material for rubber, and the control of pollutants escaping from military engines during fighter jet flight. However, the extensive use of fuel additives is hindered by the lack of knowledge about the exact mechanism of soot control. Experimental observations are limited by the obvious extreme conditions present during combustion and the fact that the additives are invariably encased in a thick carbonaceous matrix. Recently, small particles produced by the combustion process have been collected onto holey carbon covered copper grids from known positions in the flame using a thermophoretic sampling technique (Dobbins and Megaridis, 1987). This technique uses the thermophoretic forces created by introducing a cold surface into the hot gasses of the flame to force Fe particles onto the surface of the sample grid. The apparatus consists of a pneumatic cylinder which allows a probe to be inserted into the flame at a precise position and for a known length of time (typically of the order of 50 ms). Once on the grid the particles can be examined in the STEM.

Figure 7 shows low magnification Z-contrast and bright field images for particles collected from the region just above a flame tip, i.e. oxygen rich environments. It can be seen that these particles have a wide size distribution with particles ranging from about 50 nm down to 1 nm in diameter. The majority of particles are at the lower end of this size range and it is interesting to note that the smallest of the particles are barely seen in standard bright field imaging. These particles are predominantly soot-free except for a very thin (<1 nm) layer of carbon which can seen as a halo around the larger particles in the bright field images. Using the Z-contrast image to define accurately the probe position, EELS spectra have been collected from the center and surface of individual particles (Fig. 8). Significant changes at both the iron L_{23}-edge and the oxygen K-edge from the center of the particles to their edge are seen. This change in intensity ratio of the L_3 and L_2-edges may be correlated to a change in oxidation state of the iron. In practice, since the white lines sit on top of the contribution from transitions to continuum states, measurement of the white line intensity ratio is non-trivial. However, applying two different methods described in the literature (Colliex *et al.*, 1991; Pearson *et al.*, 1988), the ratio of L_3/L_2 is consistent with the center of the particles being more oxidized than the surface. The same result is obtained from analysis of the pre-edge structure of the Oxygen K-edge (Wallis *et al.*, 1996). While this seems a counter intuitive result, it should be remembered that each of the particles is encased in a carbon 'skin', and similar results have been observed for LaC_2, YC_2, α-Fe and Fe_3C particles encapsulated in carbon cages (Saito *et al.*, 1993). Atomic resolution Z-contrast images of the particles acquired using the VG HB603U imply that the center of the particles do consist of Fe_2O_3 as suggested by the EELS spectra. Fig. 9 shows lattice fringes consistent with the tetragonal phase of iron oxide, maghemite. While it is dangerous to draw any definite conclusions by matching spacings to a crystal structure, the consistency with the EELS results is gratifying. For many of the observed particles, phase boundaries similar to that seen in Fig. 9 are seen, indicating growth by the merger of two smaller particles.

Particles collected from oxygen-lacking regions within the flame are found to be very different from those collected above the flame. The particle size distribution is much narrower than the post-flame sample and the most probable particle size is also larger at about 10 nm. It can also be seen that the iron particles are contained

Fig. 7. Low magnification images of particles collected above the flame. (a) and (c) Z-contrast images, (b) and (d) bright field images. The small particles arrowed in (a) and (c) can not be seen in (b) and (d). A halo due to a fine layer of carbon may be seen around the large particle in (d).

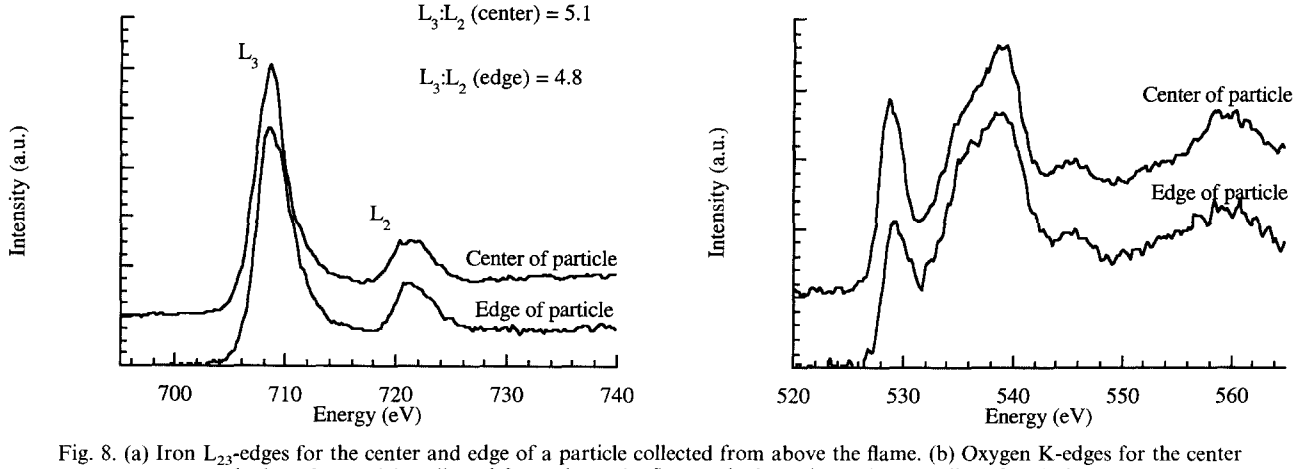

Fig. 8. (a) Iron L_{23}-edges for the center and edge of a particle collected from above the flame. (b) Oxygen K-edges for the center and edge of a particle collected from above the flame. The intensity scales are off set for clarity.

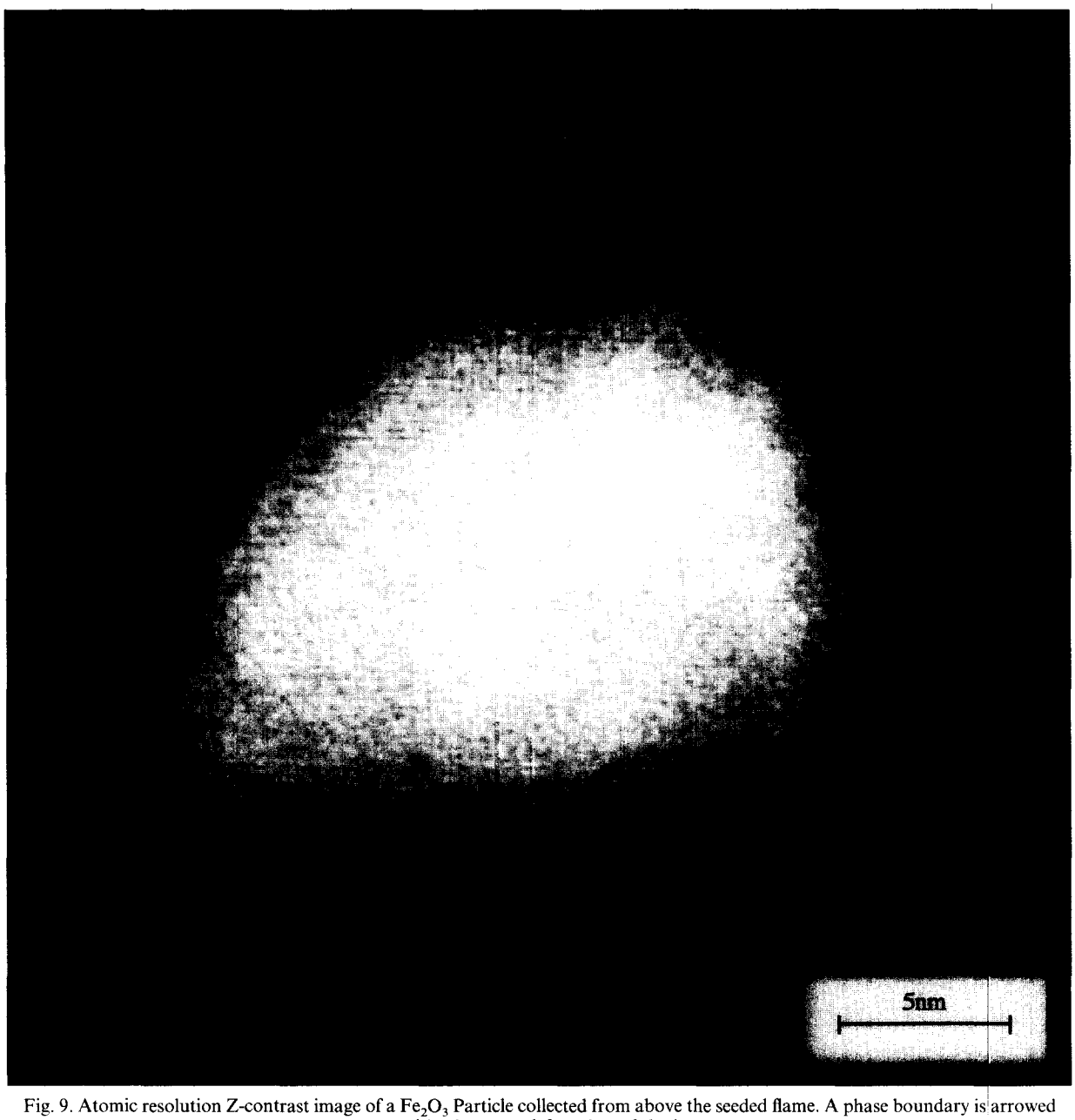

Fig. 9. Atomic resolution Z-contrast image of a Fe_2O_3 Particle collected from above the seeded flame. A phase boundary is arrowed arrowed in the upper left region of the image.

in a thick carbonaceous soot matrix. No oxygen was detected in these particles using EELS and the soot matrix was confirmed to be carbonaceous with little or no atomic iron present in it. Atomic resolution images of the particles contained within the soot (Fig. 10) also suggest that they are not iron oxide or pure iron since the spacings observed in the particles do not correlate with those of any iron oxide or pure iron phase. A possible candidate element for inclusion in these particles is obviously carbon due to its abundance in the soot matrix. However, the spacings seen in Fig. 10 could not be used to uniquely identify any single phase of iron carbide, which may indicate that the particles contain a significant amount of hydrogen and may thus be composed of an iron hydrogen carbide. However, the exact phase of this material could not be identified and it is likely that several different phases are present in these particles.

The fact that the interior of the emitted particles is found to consist completely of Fe_2O_3 and contains no carbon provides strong evidence that iron catalytically enhances the oxidation of carbon into gaseous CO and CO_2 and therefore reduces soot formation (Zhang and Megaridis, 1994). A possible route for this reaction is that the iron is first oxidized, gaseous carbon compounds condense onto the particle surface, and finally iron is reduced by carbon to form gaseous CO or CO_2. Such a sequence of reactions has been shown to be thermodynamically favorable in flame environments (Sturgen *et al.*, 1976).

3-D structural analysis of interfaces

The final application of these correlated techniques to be discussed is the use of the energy loss spectrum to

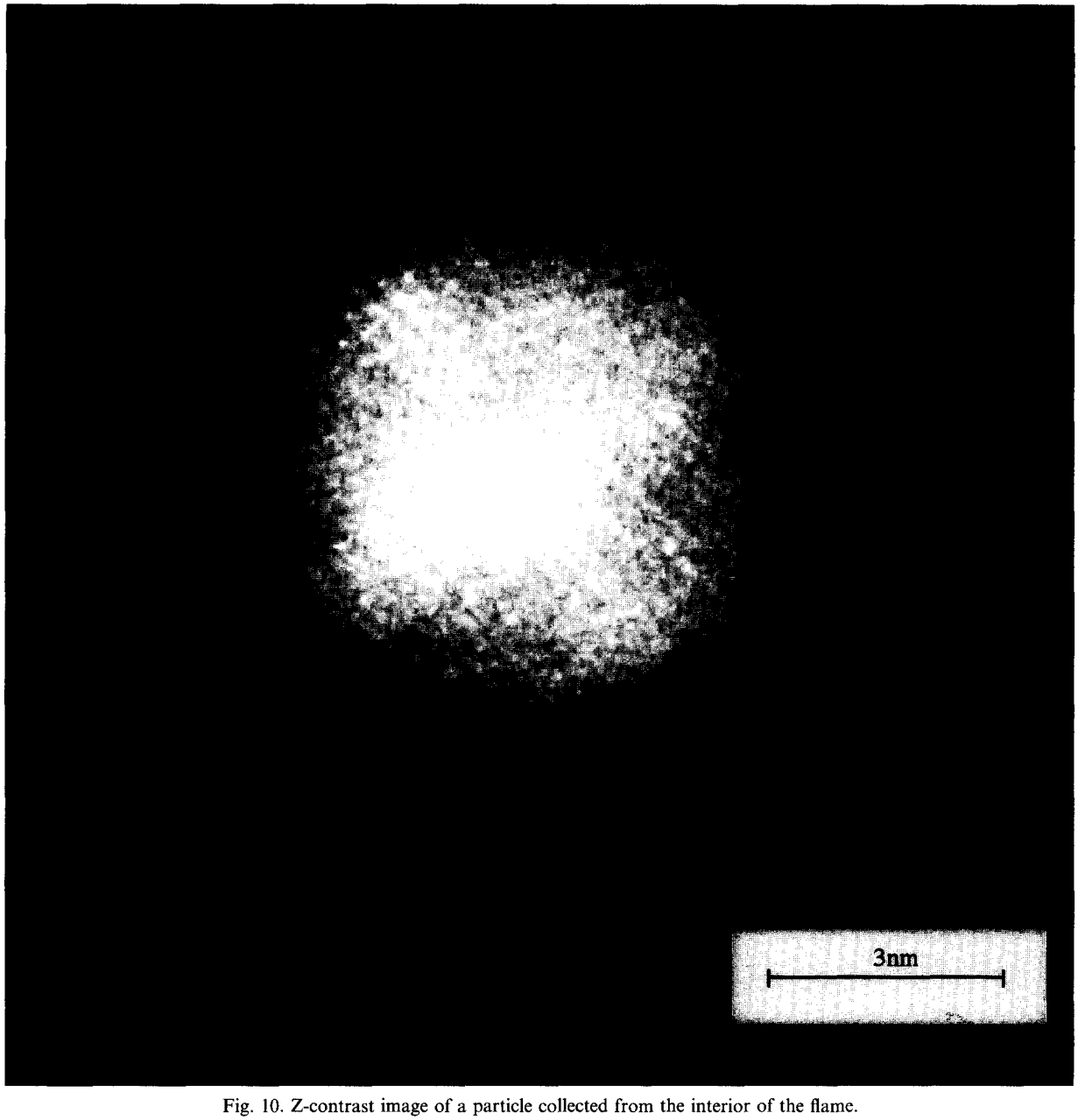

Fig. 10. Z-contrast image of a particle collected from the interior of the flame.

determine the 3-dimensional atomic structure of grain boundaries. In this case the Z-contrast image is used more than to just position the probe for microanalysis. As will be shown, the correlation of the spectral and image information leads to a determination of the grain boundary structure at a level not possible by either technique alone. Such determinations can account for the bonding at the interface and the presence of atomic vacancies.

(210) Symmetric [001] tilt boundary in TiO_2

Figure 11 shows a Z-contrast image of the Σ5 (210) tilt grain boundary in TiO_2 (rutile). The direct image provided by the Z-contrast technique makes it straightforward to propose a structure for the interface. However, interface models based only on this Z-contrast image must account for the fact that the Rutile crystal contains two Ti sub-lattices which are related to each other by a translation of 1/2[111] and a rotation of 90°. If the Ti at position (0,0,0) is labeled A and the Ti at position (1/2,1/2,1/2) labeled B, there are three possible structures for the interface plane consistent with the Z-contrast image; AA, BB and AB (Fig. 12). As the information present in the image is simply a 2-D projection of each Ti sub-lattice it is impossible to distinguish between the models from the image alone. Electron energy loss spectroscopy from the interface region allows this ambiguity in the interface structure to be resolved. Figure 13 shows experimental Oxygen K-edge spectra and titanium L-edge spectra from the bulk and the interface. The comparison of the two spectra in each case shows very little change. It therefore appears that the bonding at the interface is very similar to the bulk. This is consistent with the AB interface shown in Fig. 12.

The assignment of the AB interface as consistent with both the image and the spectrum can be confirmed by multiple scattering analysis (Wallis *et al.*, 1997b). In

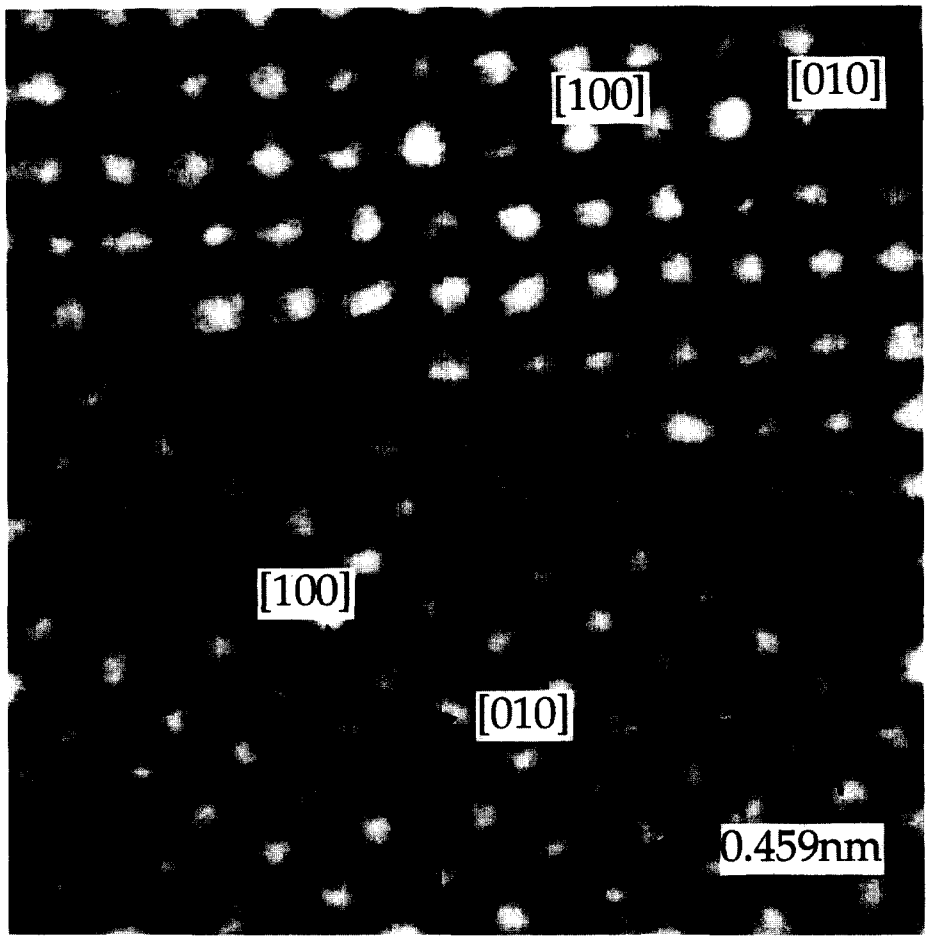

Fig. 11. Z-contrast image of a Σ5 (210) tilt grain boundary in TiO_2.

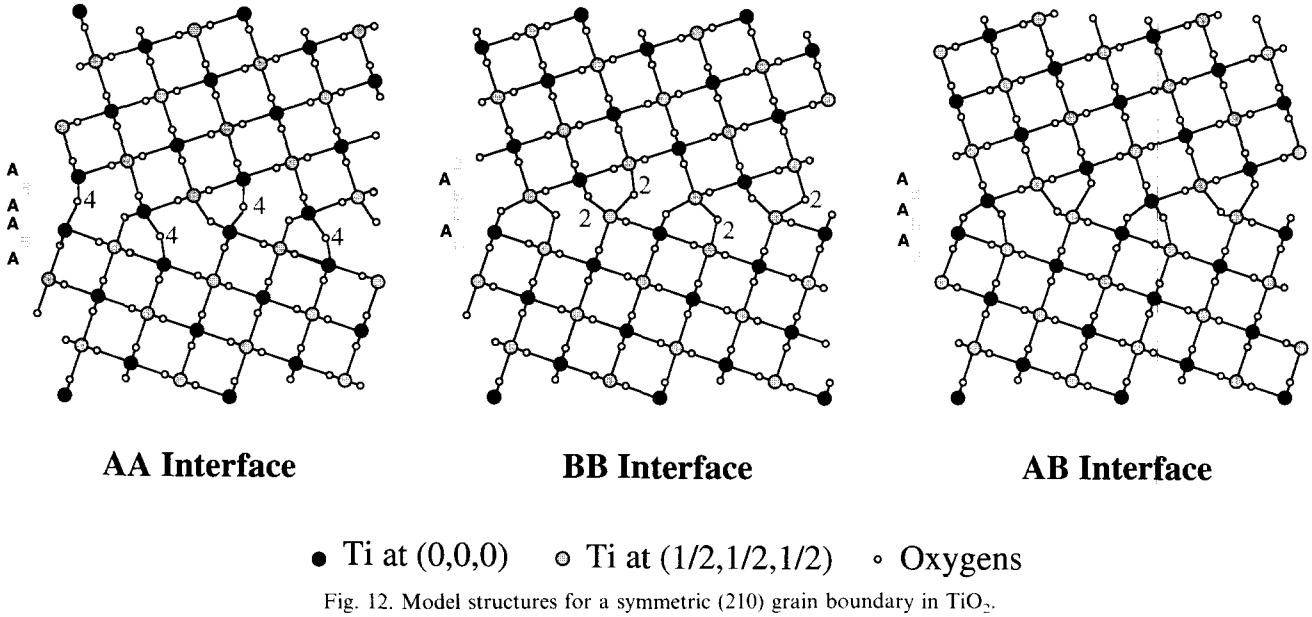

Fig. 12. Model structures for a symmetric (210) grain boundary in TiO_2.

Fig. 14, the expected energy loss spectrum for 2-fold, 3-fold and 4-fold coordinated oxygen is compared to the experimental spectrum from the interface. It can be seen that the expected spectrum from 2- and 4-fold coordinated oxygen is considerably different from the 3-fold spectrum and the experiment. The 3-fold coordinated spectrum shows good agreement with the experiment except for the splitting of the first peak. This peak is due to transitions to states involving the Ti 3d levels and the splitting of these states occurs as a result of the effects of the anisotropic crystal field at the atomic sites (i.e. crystal field splitting). Since the multiple scattering calculations are performed within the muffin tin approximation, spherical symmetry is imposed and the calculations cannot reproduce this splitting. However, it is well known that the multiple scattering technique is

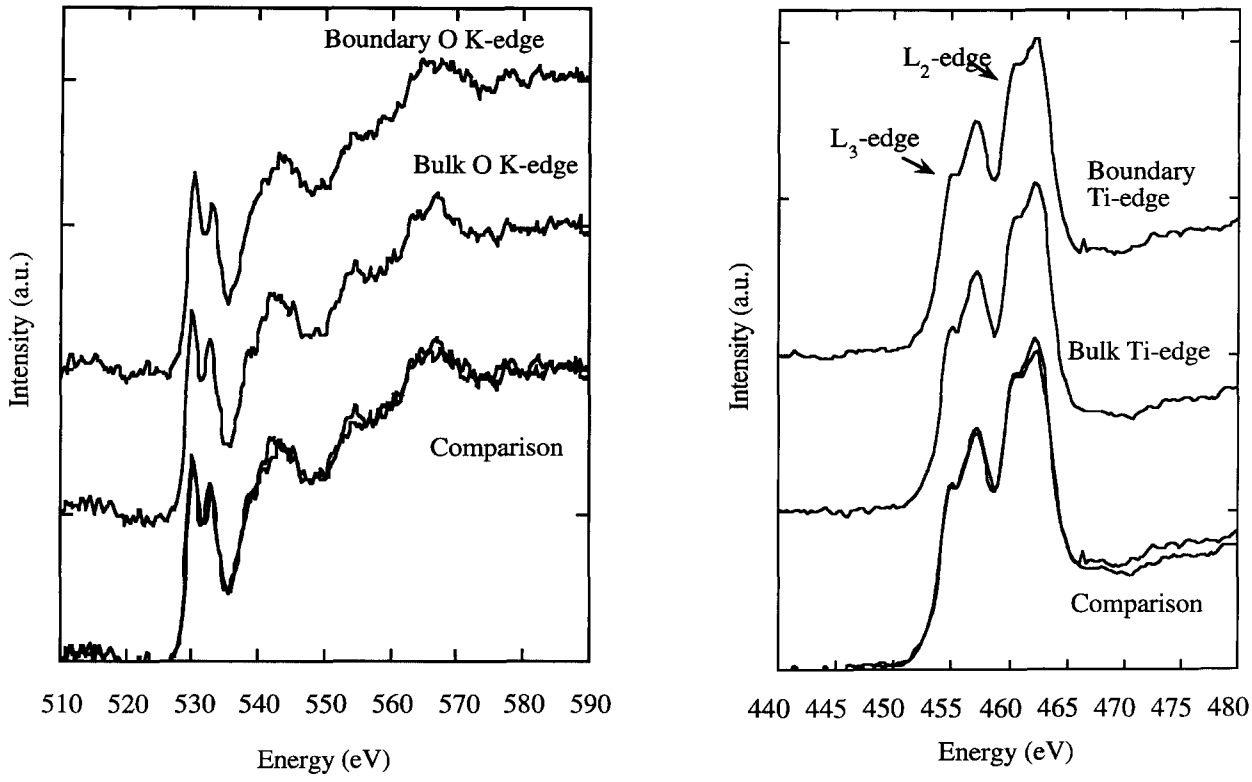

Fig. 13. (a) Oxygen K-edge spectrum collected by scanning the electron probe along the boundary plane. Also shown is a spectrum for bulk TiO_2 and a comparison between bulk and boundary spectra. (b) Ti L_{23}-edge collected by scanning the electron probe along the boundary plane. Also shown is a bulk Ti L_{23}-edge and a comparison of the two spectra.

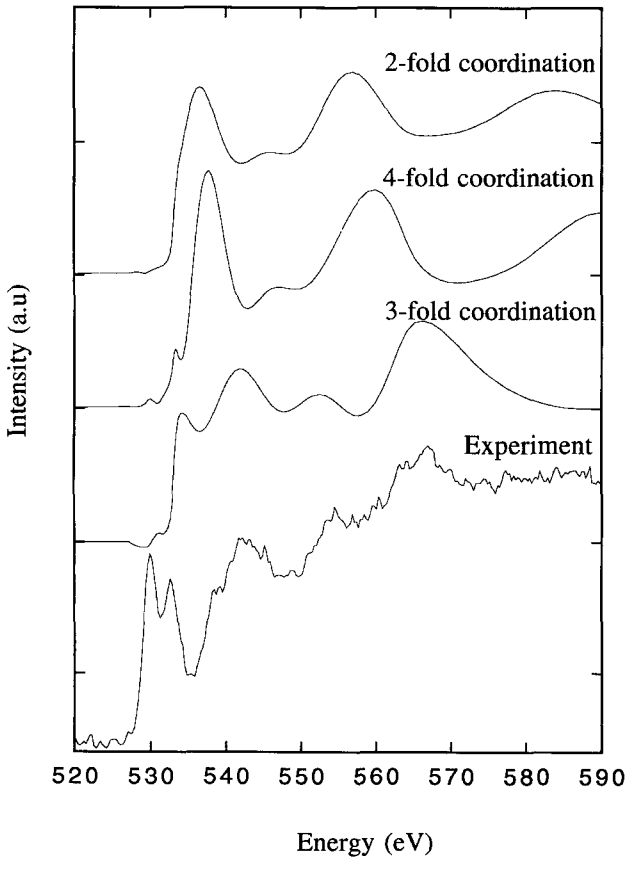

Fig. 14. (a) Multiple scattering calculations modeling the effects of (i) 2-fold coordination, (ii) 4-fold coordination and (iii) 3-fold coordination. Also shown is the experimental spectrum for comparison.

more accurate further away from the threshold and interpretation of the other peaks in the spectrum is not invalidated by the inability to reproduce the first peak.

45° Asymmetric [001] tilt boundary in $SrTiO_3$

Figure 15 shows the Z-contrast image and schematic structure of a 45° asymmetric [001] tilt grain boundary in $SrTiO_3$. Positions where the atomic columns appear too close together are highlighted in the schematic. These atomic positions are known to be real features in the image and have been postulated to be partially occupied, thus avoiding the problems of like ion repulsion (McGibbon *et al.*, 1994). This partial occupancy hypothesis can be tested by multiple scattering analysis (Wallis and Browning, 1997). The oxygen K-edge spectra and titanium L-edge spectra obtained from the bulk and boundary are shown in Fig. 16 (Browning and Pennycook, 1996). The titanium spectrum from the interface shows no change from the bulk spectrum. From this it can be determined that the valence and coordination of the titanium atoms at the boundary remains unchanged. The changes in the oxygen edge are slight, but visible on all the main peaks in the spectrum.

The multiple scattering simulation of the experimental bulk oxygen spectrum is found to reproduce the five main peaks and their relative intensities for an 8 shell cluster containing 99 atoms (Fig. 17). The fact that the intensities of some of the peaks require such a large cluster to be fully reproduced indicates that they are sensitive to long range order (particularly peak a). It is

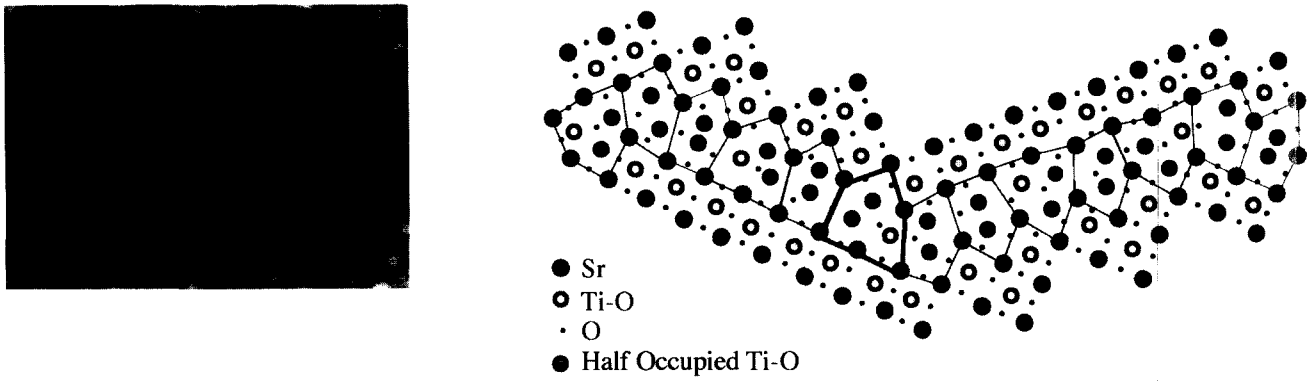

Fig. 15. (a) Z-contrast image of a 45° asymmetric [001] tilt boundary in $SrTiO_3$ (b) schematic of the boundary structure showing the presence of partially occupied sites.

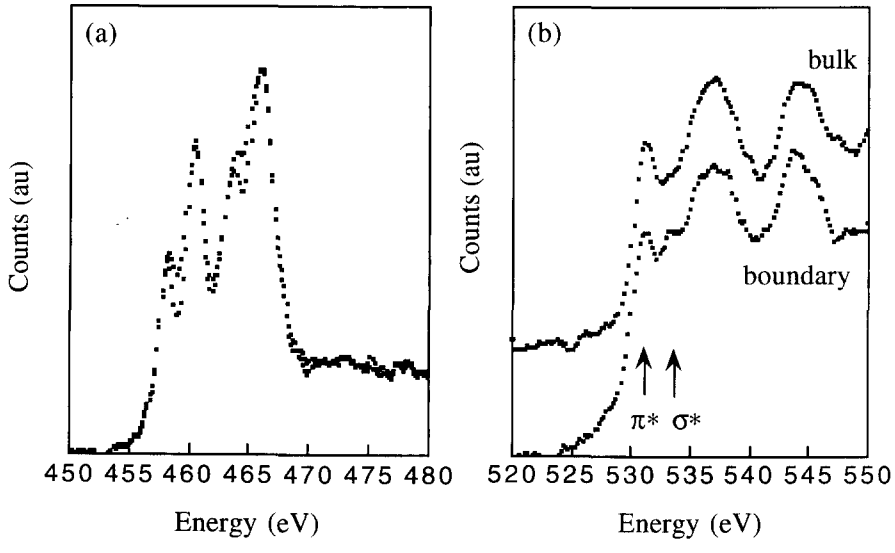

Fig. 16. (a) Ti L_{23}-edge spectrum from the bulk and boundary, (b) Oxygen K-edge spectrum from the bulk and boundary. Experimentally spectra have been acquired in a scan across the boundary in single unit cell steps. Two spectra are recorded in each position to measure any beam damage effects. Here, a single spectrum from the bulk and the boundary are shown for clarity.

therefore not surprising that the presence of the grain boundary would destroy this long range order and have an effect on the spectrum. However, using the multiple scattering formulation, it is possible to go a step further in the analysis of the spectrum and begin to address the presence of lattice vacancies in the boundary core. Such vacancies will have a markedly different effect on the fine-structure than distortions of the lattice. Distortions will generally broaden peaks by destroying the symmetry. Vacancies on the other hand will completely remove scattering paths that can lead to an enhancement or reduction in the intensity of a particular feature (depending on whether the scattering event would lead to destructive or constructive interference). Figure 17 shows the effect on the bulk spectrum of the removal of titanium, strontium and oxygen atoms from the cluster. It is apparent from these simulations that vacancies of different species have noticeably different effects on the spectrum.

Having determined the effect of vacancies on the oxygen K-edge spectrum, we are now in a position to interpret the changes seen in the experimental spectrum from the grain boundary. Figure 18 compares the changes seen experimentally with the changes in the oxygen K-edge spectra obtained from two clusters. The first cluster contains the bulk structure of $SrTiO_3$, While the second cluster contains 4 oxygen vacancies. This number of vacancies reproduces the changes in the 5 peak positions and intensities seen experimentally by moving from the bulk to the boundary. At first glance it is not obvious why the experimental spectra are reproduced by the incorporation of oxygen vacancies when the image infers partial occupancy of the titanium sites. However, we know from the titanium L-edge spectrum that even with partial occupancy the titanium atoms must maintain the bulk valence and coordination. The only way for this to occur at the boundary is for the partially occupied titanium columns to be accompanied by oxygen vacancies.

CONCLUSIONS

The combination of EELS and Z-contrast imaging in the STEM can be used to determine the structure, composition, chemistry and bonding of materials with atomic resolution and sensitivity. Such capabilities make it possible to investigate the structure-property

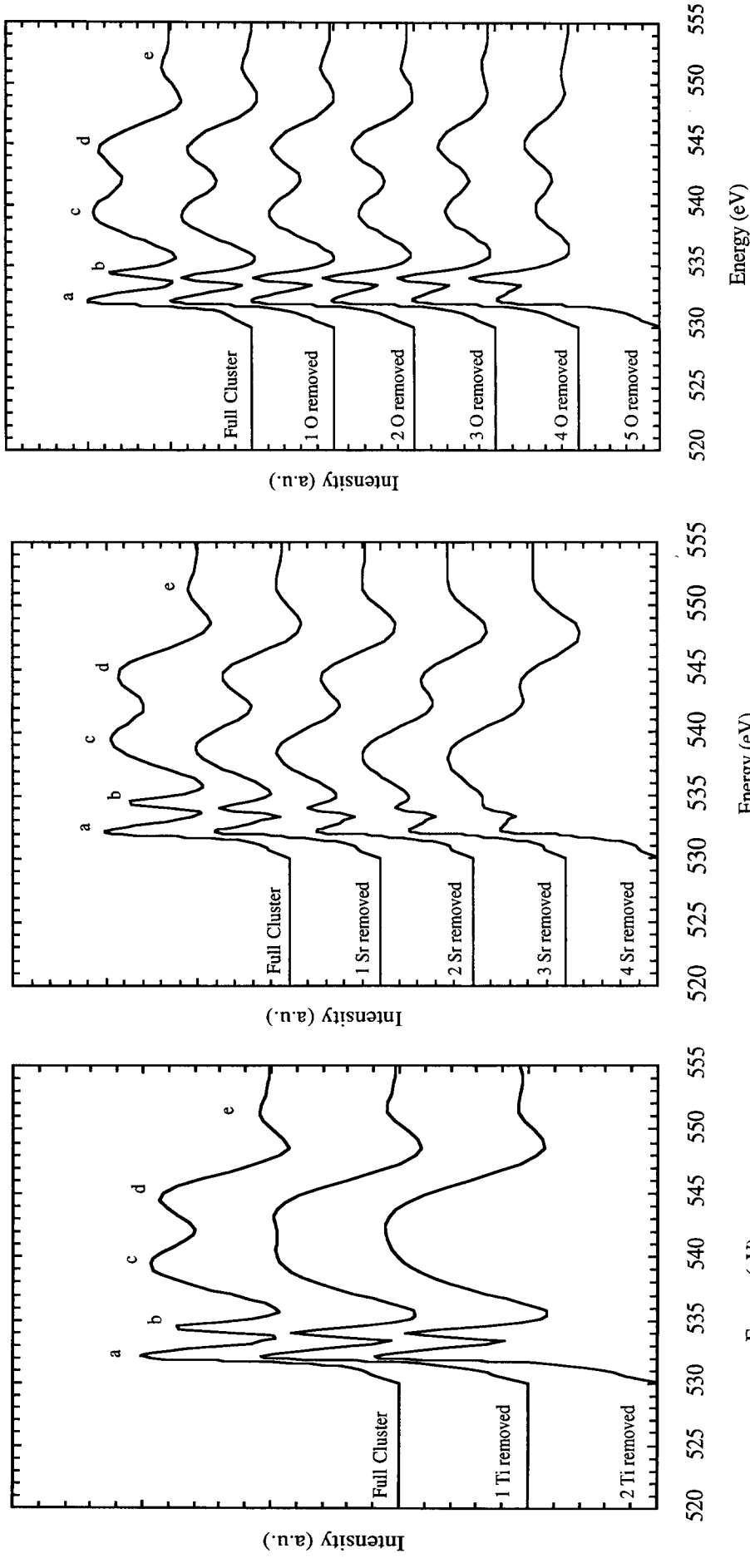

Fig. 17. Multiple scattering simulations of the effects of (a) Ti (b) Sr and (c) oxygen vacancies. These features can be correlated with the experimentally observed changes in the spectrum at the boundary.

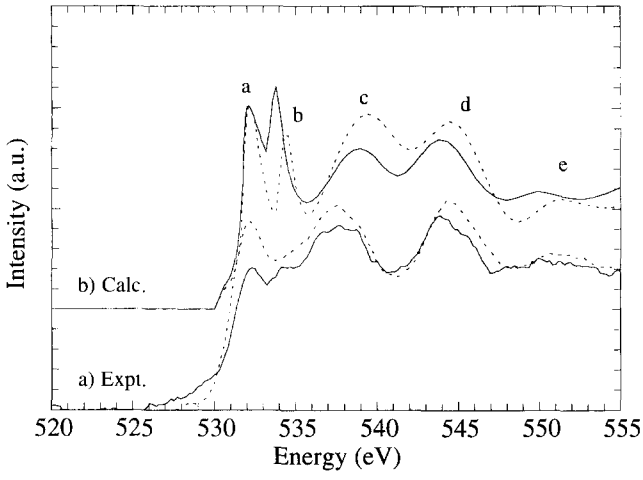

Fig. 18. Comparison of experimental and simulated spectra from the bulk (dashed line) and boundary (solid line). The experimental shift in peak positions and intensity changes are best modelled by considering the presence of 4 oxygen vacancies in the cluster.

relationships of materials and devices on the fundamental atomic scale. The application of these techniques in the STEM avoids the problems of lens aberration, signal coherence, low-signal, beam damage and specimen drift associated with energy filtered TEM images and spectrum images in STEM. The limit to the resolution of these techniques for crystalline materials is the probe size. While a probe small enough for atomic resolution has been a capability unique to VG microscopes, the recent development of sub−0.2 nm probes in commercially available 200 kV Field-emission TEM's from other manufacturers suggests the use of these techniques will become more widespread.

Acknowledgements—Aspects of this work were performed in collaboration with S. Sivananthan, C. M. Megaridis, I. Majid, Y. Liu and J. B. Vander Sande. The authors are grateful to J. T. Luck and J. Zhang for technical assistance. This research is funded by NSF under grant No. DMR-9503877, by the US DOE under contract no. DE-ACOS-96OR22464 with Lockheed Martin Energy Research Corporation and by an appointment to the ORNL postdoctoral program administered by ORISE.

REFERENCES

Allen, L. J. and Rossouw, C. J., 1990. Absorptive potentials due to ionisation and thermal diffuse scattering by fast electrons. *Phys Rev*, **B 42,** 11644–11654.

Batson, P. E., 1993. Simultaneous STEM and electron energy loss spectroscopy with atomic column sensitivity. *Nature*, **366,** 727–729.

Benfatto, M., Natoli, C. R., Bianconi, A., Garcia, J., Marcelli, A., Fanfoni, M. and Davoli, I., 1986. *Phys. Rev.*, **B 34,** 5774.

Brown, L. M., 1981. Scanning transmission electron microscopy: Microanalysis for the microelectronic age. *J. Phys*, **F 11,** 1–26.

Browning, N. D. and Pennycook, S. J., 1993. Atomic Resolution Spectroscopy for the Microanalysis of Materials. *Microbeam Analysis*, **2,** 81–89.

Browning, N. D., Chisholm, M. F. and Pennycook, S. J., 1993. Atomic Resolution Chemical Analysis in the Scanning Transmission Electron Microscope. *Nature*, **366,** 143–146.

Browning, N. D. and Pennycook, S. J., 1996. Direct Experimental Determination of the Atomic Structure at Internal Interfaces. *J. Phys*, **D 29,** 1779–1798.

Brydson, R., Sauer, H. and Engle, W., 1992. Electron Energy Loss Near Edge structure as an Analytical Tool-The Study of Minerals. In *Transmission Electron Energy Loss Spectrometry in Materials Science*, ed. M. M. Disko, C. C. Ahn and B. Fultz, pp. 131–154, The Minerals, Metals and Materials Society, Warrendale, PA.

Chen, Y. P., Faurie, J. P., Sivananthan, S., Hua, G. C. and Otsuka, N., 1995. *J. Electronic Materials*, **24,** 475.

Colliex, C. and Mory, C., 1984. Quantitative aspects of scanning transmission electron microscopy. In *Quantitative Electron Microscopy*, eds. J. N. Chapman and A. J. Craven, pp. 149–216, SUSSP publications, Edinburgh, UK.

Colliex, C., Manoubi, T. and Ortiz, C., 1991. Electron-energy-loss-spectroscopy near-edge fine structures in the iron-oxygen system. *Phys. Rev.*, **B 44,** 11402–11411.

Disko, M. M., Ahn, C. C. and Fultz, B., 1992. Transmission Electron Energy Loss Spectrometry. In *Materials Science*, The Minerals, Metals and Materials Society, Warrendale, PA.

Dobbins, R. A. and Megaridis, C. M., 1987. Morphology of flame generated soot as determined by thermophoretic sampling. *Langmuir*, **3,** 254–259.

Egerton, R. F., 1986. *Electron Energy Loss Spectroscopy in the Electron Microscope*, Plenum Press, New York.

Fertig, J. and Rose, H., 1981. *Optik*, **59,** 407.

Holbrook, O. F. and Bird, D. M., 1995. *Proc. Microscopy and Microanalysis*, **1995,** 278–279.

Jesson, D. E. and Pennycook, S. J., 1993. Incoherent Imaging of Thin Specimens using Coherently Scattered Electrons. *Proc. R. Soc. Lond.*, **A 441,** 261–281.

Koningsberger, D. C., 1987. X-ray absorption: Principles. In *Applications, Techniques of EXAFS, SEXAFS and XANES*, eds. D. C. Koningsberger and R. Prins, Wiley, New York.

Loane, R. F., Kirkland, E. J. and Silcox, J., 1988. Visibility of single heavy atoms on thin crystalline silicon in simulated annular dark field STEM images. *Acta. Cryst.*, **A44,** 912–927.

Loane, R. F., Xu, P. and Silcox, J., 1992. *Ultramicroscopy*, **40,** 121.

Mattheiss, L., 1964. Energy Bands for Solid Argon. *Phys. Rev.*, **A 133,** 1399.

McGibbon, M. M., Browning, N. D., Chisholm, M. F., Pennycook, S. J., Ravikumar, V. and Dravid, V. P., 1994. Direct Determination of Grain Boundary Atomic Structure in $SrTiO_3$. *Science*, **266,** 102–104.

McMullan, D., Mooroka, Y. and Fallon, P., 1990. Parallel Electron Energy Loss Spectroscopy. *Inst. Phys. Conf Ser.*, **98,** 55–61.

Pearson, D. H., Fultz, B. and Ahn, C. C., 1988. Measurements of 3d state occupancy in transition metals using electron energy loss spectroscopy. *Appl. Phys. Lett.*, **53,** 1405–1407.

Pennycook, S. J. and Boatner, L. A., 1988. *Nature*, **336,** 565–567.

Pennycook, S. J. and Jesson, D. E., 1991. High-resolution Z-contrast Imaging of Crystals. *Ultramicroscopy*, **37,** 14–38.

Pennycook, S. J. and Jesson, D. E., 1990. High Resolution Incoherent Imaging of Crystals. *Phys. Rev. Lett.*, **64,** 938–941.

Pennycook, S. J., Jesson, D. E. and Browning, N. D., 1995. Atomic-Resolution Electron Energy Loss Spectroscopy in Crystalline Solids. *Nucl. Inst and Methods*, **96,** 575–582.

Rehr, J. J., Zabinsky, S. I. and Albers, R. C., 1992. High-Order Multiple-Scattering Calculations of X-Ray-Absorption Fine Structure. *Phys. Rev. Lett.*, **69,** 3397–3400.

Rez, P., 1992. Energy Loss Fine Structure. In *Transmission Electron Energy Loss Spectrometry in Materials Science*, eds. M. M. Disko, C. C. Ahn and B. Fultz, pp. 107–130, The Minerals, Metals and Materials Society, Warrendale, PA.

Ritchie, R. H. and Howie, A., 1988. Inelastic scattering probabilities in scanning transmission electron microscopy. *Philosophical Magazine*, **58,** 753–767.

Saito, Y., Yoshikawa, T., Okuda, M., Fujimoto, N., Yamamuro, S., Wakoh, K., Sumiyama, K., Suzuki, K., Kasuya, A. and Nishina, Y., 1993. Iron particles nesting in carbon cages grown by arc discharge. *Chem. Phys. Lett.*, **212,** 379–383.

Sturgen, R. E., Chakrabati, C. L. and Langford, C. H., 1976. Studies on the mechanism of atom formation in graphite furnace atomic absorption spectroscopy. *Anal. Chem.*, **48,** 1792–1807.

Taftø, J. and Krivanek, O. L., 1982. Characteristic energy-loss from channeled 100keV electrons. *Nucl. Instrum. Methods*, **194,** 153–158.

Tossell, J. A., 1973. *Geochem. Cosmochim Acta*, **37,** 583.

Wallis, D. J., Browning, N. D., Megaridis, C. M. and Nellist, P. D., 1996. Analysis of nanometer sized pyrogenic particles in the scanning transmission electron microscope. *J. Microscopy*, **184,** 185–194.

Wallis, D. J. and Browning, N. D., 1997. Probing vacancies and structural distortions at ceramic grain boundaries with atomic resolution electron energy loss spectroscopy. *J. Am. Ceram. Soc,* **80,** 781–785.

Wallis, D. J., Browning, N. D., Nellist, P. D., Pennycook, S. J., Majid, I., Liu, Y. and Vander Sande, J. B., 1997. Atomic structure of a 36.8° (210) tilt grain boundary in TiO_2. *J. Am. Ceram. Soc,* **80,** 499–502.

Wallis, D. J., Browning, N. D., Sivananthan, S., Nellist, P. D. and Pennycook, S. J., 1997b. *Appl. Phys. Letts.* (in press).

Yoshikawa, S. A., Nogami, J., Quate, C. F. and Pianetta, P., 1994. *Surface Science,* **321,** L183.

Zhang, J. and Megaridis, C. M., 1994. *Iron/soot interaction in a laminar ethylene nonpremixed flame*, pp. 593–600, 25th Symposium on Combustion/The Combustion Institute.